

Efficient mesh refinement for the Poisson-Boltzmann equation with boundary elements

Vicente Ramm*, Jehanzeb H. Chaudhry[†], Christopher D. Cooper[‡]

December 14, 2021

Abstract

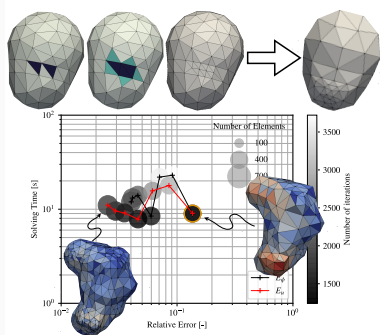
The Poisson-Boltzmann equation is a widely used model to study the electrostatics in molecular solvation. Its numerical solution using a boundary integral formulation requires a mesh on the molecular surface only, yielding accurate representations of the solute, which is usually a complicated geometry. Here, we utilize adjoint-based analyses to form two goal-oriented error estimates that allows us to determine the contribution of each discretization element (panel) to the numerical error in the solvation free energy. This information is useful to identify high-error panels to then refine them adaptively to find optimal surface meshes. We present results for spheres and real molecular geometries, and see that elements with large error tend to be in regions where there is a high electrostatic potential. We also find that even though both estimates predict different total errors, they have similar performance as part of an adaptive mesh refinement scheme. Our test cases suggest that the adaptive mesh refinement scheme is very effective, as we are able to reduce the error one order of magnitude by increasing the mesh size less than 20%. This result sets the basis towards efficient automatic mesh refinement schemes that produce optimal meshes for solvation energy calculations.

Keywords: Poisson-Boltzmann, Implicit solvent, Goal-oriented adjoint based error estimation, Boundary element method, Adaptive mesh refinement. ■

*Departamento de Ingeniería Mecánica, Universidad Técnica Federico Santa María

[†]Department of Mathematics and Statistics, University of New Mexico

[‡]Departamento de Ingeniería Mecánica and Centro Científico Tecnológico de Valparaíso (CCTVal), Universidad Técnica Federico Santa María, Valparaíso, Chile



The Poisson-Boltzmann equation is widely used to compute solvation energies of molecules. It considers the solute as a cavity region in an infinite dielectric, interfaced by the molecular surface. The boundary element method offers an efficient numerical solution, as it discretizes the interface only. Here, we present an *a posteriori* error estimation method that detects high error elements, with which we generate a highly effective adaptive mesh refinement technique.

INTRODUCTION

In biological settings, biomolecules are found immersed in water with salt, and an appropriate treatment of the solvent is key to have accurate models. A popular treatment considers the solvent implicitly, where rather than accounting for each water molecule in a discrete way, they are represented as a continuum material^{1,2}. The implicit solvent model represents molecules in solution with continuum electrostatic theory, where a solute (region Ω_m) is surrounded by an infinite dielectric (region Ω_w), as sketched by figure 1. The solute is a region without water or salt, where the dielectric constant is low ($\epsilon_m = 2 - 4$), and contains partial charges that are represented as point-delta functions. Outside the solute, we use the permittivity of water ($\epsilon_w = 80$), and consider the presence of salt (κ). These two regions are interfaced by a molecular surface or interface (Γ), where several definitions are possible³: solvent-excluded, solvent-accessible, Gaussian, or van der Waals surface. In this work, we use the solvent-excluded surface⁴, which is the result of rolling a spherical probe of the size of a water molecule (1.4 Å radius), and tracking the contact points between the probe and the atoms of the solute (with their corresponding van der Waals radii).

This implicit solvent approximation dramatically reduces the number of degrees of freedom compared to molecular dynamics, and yields a partial differential equation (PDE) based model. If we consider that, at equilibrium, the mobile ions from the salt in the solvent arrange according to Boltzmann’s distribution, electrostatic theory results in the so-called Poisson-Boltzmann equation (PBE). A common quantity of interest is the solvation free energy, which is the work required to bring the solute molecule from vacuum into its solvated state. The focus of this article is then twofold:

- i Derive accurate a posteriori estimates for the error in a boundary element method approximation of the solvation free energy.
- ii Design an adaptive mesh refinement algorithm to efficiently arrive at accurate solutions.

The PBE has been solved numerically with a wide variety of techniques, such as finite difference⁵⁻⁷, finite element⁸⁻¹⁰, and boundary element (BEM)¹¹⁻¹⁴ methods. In particular, BEM uses a surface integral formulation¹⁵⁻¹⁷, where only the solute-solvent interface is discretized, and the potential goes to zero at infinity by construction. Then, the molecular

surface is accurately represented, making BEM favorable for high precision simulations¹⁴. However, BEM generates dense matrices that need fast methods to access large problems, such as fast multipole methods^{18,19}, treecodes^{20,21}, or hierarchical matrices^{22,23}.

Numerical approximations to the PBE often have large error. Hence, for the reliable use of the PBE in science and engineering, this error needs to be quantified. The tool used to accomplish this task in this article is adjoint based error estimation. In this technique, one solves an adjoint problem whose solution provides the residual weighting to produce the error in the goal functional. The resulting estimate also allows to identify the contributions to the error due to an individual mesh element (panel) and hence aid in forming adaptive algorithms.

Adjoint based analysis has been used for the error estimation of a variety of numerical methods and differential equations^{24–27}, for example, finite element methods^{28–31}, finite volume methods³², numerous time-integration schemes^{33–37}, and parallel-in-time and domain decomposition methods^{38,39}. A posteriori analysis of the finite element method for the PBE has been considered previously^{40,41}, however, this work is the first such analysis for the PBE with BEM. Residual based a posteriori analysis for BEM has been studied earlier^{42,43}, however, they focused on error in some global norm of the solution, whereas here we focus on quantifying the error in a goal functional or quantity of interest. Moreover, if the aim of the computation is to minimize the error in the goal, then forming per-element contributions of the error in the goal is a crucial ingredient in designing an adaptive algorithm. We achieve this aim by combining information from the numerical solution of the PBE with adjoint solutions to classify mesh elements that contribute the most towards the error in the goal. These elements are then refined to decrease the error in numerical approximations of the goal functional.

In the next section, we present the methodology, including the equations governing the implicit solvent model, the boundary integral formulation for the PBE, and finally derive two error estimates using adjoint based error analysis. The error estimates are also used to form per-element error indicator to devise a local mesh refinement strategy. In the Results and Discussion section we test the performance of the error estimates and the mesh refinement strategy on a variety of molecular setups. Finally, the last section presents the conclusions

and outlook for future work.

METHODOLOGY

The Poisson-Boltzmann equation and Solvation Free Energy

BEM is limited to linear problems, however, the linearized version of the PBE is sufficiently accurate for most protein problems, where charges and potentials are not high⁴⁴. The linearized PBE is

$$-\nabla \cdot (\epsilon(\mathbf{r})\nabla u(\mathbf{r})) + \bar{\kappa}^2(\mathbf{r})u(\mathbf{r}) = \sum_{k=1}^{N_q} q_k \delta(|\mathbf{r} - \mathbf{r}_k|) \quad (1)$$

where q_k is the partial charge of atom k (located at \mathbf{r}_k), $\epsilon(\mathbf{r})$ is the permittivity, and $\bar{\kappa}(\mathbf{r}) = \kappa\sqrt{\epsilon_w}$ is the modified Debye-Hückel parameter, with κ the inverse of the Debye length. Here, we use $\kappa = 0.125 \text{ \AA}^2$ in the solvent region, which corresponds to NaCl dissolved in water at a concentration of 150mM, while we set $\kappa = 0$ in the solute region to indicate ion exclusion there. The dielectric constant also takes two values, ϵ_w or ϵ_m , depending on the region (Ω_w or Ω_m). On the interface (Γ), the potential and electric displacement are continuous:

$$[[u]]_{\Gamma} = 0, \quad \left[\left[\epsilon \frac{\partial u}{\partial \mathbf{n}} \right] \right]_{\Gamma} = 0, \quad (2)$$

where $[[\psi]]_{\Gamma} = \lim_{\alpha \rightarrow 0^+} (\psi(x + \alpha \mathbf{n}) - \psi(x - \alpha \mathbf{n}))$ is the jump in ψ across the interface, for $x \in \Gamma$, and \mathbf{n} a normal vector pointing out of Ω_m .

The electrostatic component of the solvation free energy can be computed as

$$\Delta G_{solv} = \frac{1}{2} \int_{\Omega} \rho(\mathbf{r}) u_r(\mathbf{r}) d\mathbf{r} = \frac{1}{2} \sum_{k=1}^{N_q} q_k u_r(\mathbf{r}_k) \quad (3)$$

where u_r is the so called reaction potential, due to the polarization of the solvent. Physically, the reaction potential u_r is the difference in electrostatic potential between the isolated and dissolved states (see figure 2). In the isolated state, the electrostatic potential in the solvent is exactly zero, whereas in the molecule it is the Coulomb potential from the partial charges:

$$u_c(\mathbf{r}) = \frac{1}{\epsilon_m} \sum_{k=1}^{N_q} \frac{q_k}{4\pi|\mathbf{r} - \mathbf{r}_k|}, \quad (4)$$

Then, when we take the difference in electrostatic potential, we only need to subtract out u_c in the solute region, giving

$$u_r(\mathbf{r}) = \begin{cases} u - u_c & \text{if } \mathbf{r} \text{ in } \Omega_m \\ u & \text{if } \mathbf{r} \text{ in } \Omega_w. \end{cases} \quad (5)$$

Hence, the equation, boundary condition, and jump conditions at the interface Γ for u_r are

$$\begin{aligned} -\nabla \cdot (\epsilon(\mathbf{r}) \nabla u_r(\mathbf{r})) + \bar{\kappa}^2(\mathbf{r}) u_r(\mathbf{r}) &= 0 \\ u_r(\infty) &= 0 \\ \llbracket u_r \rrbracket_\Gamma &= u_c(\mathbf{r}_\Gamma) \\ \left[\left[\epsilon(\mathbf{r}) \frac{\partial u_r}{\partial \mathbf{n}} \right] \right]_\Gamma &= \epsilon_m \frac{\partial u_c}{\partial \mathbf{n}}(\mathbf{r}_\Gamma) \end{aligned} \quad (6)$$

In practice, there is no need to calculate u_r in Ω_w for ΔG_{solv} in equation (3).

A boundary integral formulation of the Poisson-Boltzmann equation

Equation (1) is effectively a coupled system of constant coefficient partial differential equations, where the Poisson-Boltzmann equation governs in Ω_w and the Poisson equation with point-charge sources in Ω_m . Using Green's second identity, the electrostatic potential anywhere can be computed as

$$\begin{aligned} u(\mathbf{r}) &= - \oint_\Gamma u^-(\mathbf{r}') \frac{\partial}{\partial \mathbf{n}} \left(\frac{1}{4\pi|\mathbf{r} - \mathbf{r}'|} \right) d\mathbf{r}' + \oint_\Gamma \frac{\partial u^-(\mathbf{r}')}{\partial \mathbf{n}} \frac{1}{4\pi|\mathbf{r} - \mathbf{r}'|} d\mathbf{r}' + \frac{1}{\epsilon_m} \sum_{k=1}^{N_q} \frac{q_k}{4\pi|\mathbf{r} - \mathbf{r}_k|} \text{ in } \Omega_m, \\ u(\mathbf{r}) &= \oint_\Gamma u^+(\mathbf{r}') \frac{\partial}{\partial \mathbf{n}} \left(\frac{e^{-\kappa|\mathbf{r} - \mathbf{r}'|}}{4\pi|\mathbf{r} - \mathbf{r}'|} \right) d\mathbf{r}' + \oint_\Gamma \frac{\partial u^+(\mathbf{r}')}{\partial \mathbf{n}} \frac{e^{-\kappa|\mathbf{r} - \mathbf{r}'|}}{4\pi|\mathbf{r} - \mathbf{r}'|} d\mathbf{r}' \text{ in } \Omega_w, \end{aligned} \quad (7)$$

where the superscripts “ $-$ ” and “ $+$ ” indicate that the potential is being evaluated on the internal and external side of Γ , respectively. Evaluating \mathbf{r} on Γ and enforcing the interface conditions in equation (2), this becomes¹⁶

$$\begin{aligned} \frac{u^-(\mathbf{r})}{2} + \oint_\Gamma u^-(\mathbf{r}') \frac{\partial}{\partial \mathbf{n}} \left(\frac{1}{4\pi|\mathbf{r} - \mathbf{r}'|} \right) d\mathbf{r}' - \oint_\Gamma \frac{\partial u^-(\mathbf{r}')}{\partial \mathbf{n}} \frac{1}{4\pi|\mathbf{r} - \mathbf{r}'|} d\mathbf{r}' &= \frac{1}{\epsilon_m} \sum_{k=1}^{N_q} \frac{q_k}{4\pi|\mathbf{r} - \mathbf{r}_k|}, \\ \frac{u^-(\mathbf{r})}{2} - \oint_\Gamma u^-(\mathbf{r}') \frac{\partial}{\partial \mathbf{n}} \left(\frac{e^{-\kappa|\mathbf{r} - \mathbf{r}'|}}{4\pi|\mathbf{r} - \mathbf{r}'|} \right) d\mathbf{r}' + \frac{\epsilon_m}{\epsilon_w} \oint_\Gamma \frac{\partial u^-(\mathbf{r}')}{\partial \mathbf{n}} \frac{e^{-\kappa|\mathbf{r} - \mathbf{r}'|}}{4\pi|\mathbf{r} - \mathbf{r}'|} d\mathbf{r}' &= 0. \end{aligned} \quad (8)$$

where integrals are now principal value integrals.

To compute u_r in Ω_m , we use equation (7) and subtract out u_c

$$u_r(\mathbf{r}) = u^- - u_c = - \oint_{\Gamma} u^-(\mathbf{r}') \frac{\partial}{\partial \mathbf{n}} \left(\frac{1}{4\pi|\mathbf{r} - \mathbf{r}'|} \right) d\mathbf{r}' + \oint_{\Gamma} \frac{\partial u^-(\mathbf{r}')}{\partial \mathbf{n}} \frac{1}{4\pi|\mathbf{r} - \mathbf{r}'|} d\mathbf{r}'. \quad (9)$$

We solve the system in equation (8) numerically using a boundary element method (BEM), available in the **bempp** library⁴⁵. The BEM uses a triangulated surface to generate a finite dimensional representation of u^- , which we call U^- , on panel p , of the form

$$U^-(\mathbf{r}_p) = \sum_{l=1}^{N_l} \Psi(\mathbf{r}_p, \mathbf{r}_l) U^-(\mathbf{r}_l) \quad (10)$$

where Ψ is the shape function, which in this work may belong to the space of piecewise constant (for equation (8)) or linear (to solve the adjoint in equation (16)) functions. The **bempp** library uses a Galerkin discretization to arrive to a linear system for U^- and $\frac{\partial U^-}{\partial \mathbf{n}}$, which is solved using GMRES. Then, we replace these results in equation (9) to compute U_r (the numerical approximation of u_r), and then the numerical approximation of solvation energy $\Delta \hat{G}_{solv}$ as

$$\Delta \hat{G}_{solv} = \sum_{k=1}^{N_q} q_k U_r(\mathbf{r}_k) \quad (11)$$

In this BEM implementation, the surface Γ is discretized in N_p flat triangular panels using **msms**⁴⁶ or **Nanoshaper**⁴⁷, we assume a piecewise constant ansatz, and compute integrals with Gaussian quadrature rules, to obtain the numerical approximations U^- and $\frac{\partial U^-}{\partial \mathbf{n}}$ on the interface. Also, we set the GMRES tolerance to 10^{-8} in all tests.

Goal-oriented error estimation

In this work, we use an adjoint-based error estimation method, which allows us to approximate the contribution of each element to the error in a goal or quantity of interest (QoI). In general, let us consider the QoI as

$$\text{QoI} = \int_{\Omega} \psi(\mathbf{r}) u_r(\mathbf{r}) d\mathbf{r}, \quad (12)$$

where $\psi(\mathbf{r})$ is a weight function chosen to specify the QoI. Here, the QoI is the solvation free energy (ΔG_{solv}). Comparing equation (12) with the expression for the solvation free energy

in equation (3) we see that $\psi(\mathbf{r})$ is the charge distribution,

$$\psi(\mathbf{r}) = \rho(\mathbf{r}). \quad (13)$$

Note that we ignored the factor $1/2$ present in equation (3) when defining ψ . It is trivial to account for this constant factor when forming error estimates, and the error estimates we form later do indeed account for this.

The adjoint operator

Given a differential operator \mathcal{D} , the adjoint operator, \mathcal{D}^* , is defined as,

$$\int_{\Omega} \mathcal{D}w(\mathbf{r})v(\mathbf{r})d\mathbf{r} = \int_{\Omega} w(\mathbf{r})\mathcal{D}^*v(\mathbf{r})d\mathbf{r}, \quad (14)$$

where w and v are functions for $\mathbf{r} \in \Omega$. We can write $\psi(\mathbf{r})$ in terms of an adjoint function (ϕ) as

$$\mathcal{D}^*\phi(\mathbf{r}) = \psi(\mathbf{r}). \quad (15)$$

The corresponding differential operator on the adjoint is⁴⁰

$$\mathcal{D}^*\phi(\mathbf{r}) = -\nabla \cdot (\epsilon(\mathbf{r})\nabla\phi(\mathbf{r})) + \bar{\kappa}^2\phi(\mathbf{r}) = \psi(\mathbf{r}) \quad \text{in } \Omega, \quad (16)$$

which implies the following jump conditions at the interface

$$\begin{aligned} \llbracket \phi(\mathbf{r}) \rrbracket_{\Gamma} &= 0, \\ \left[\left[\epsilon(\mathbf{r}) \frac{\partial \phi}{\partial \mathbf{n}}(\mathbf{r}) \right] \right]_{\Gamma} &= 0. \end{aligned} \quad (17)$$

Exact Error Representations

Let $e_r = u_r - U_r$ denote the error in the reaction potential. Our aim is to compute the error in the numerical approximation to the solvation energy,

$$\frac{1}{2} \int_{\Omega} e_r(\mathbf{r})\psi(\mathbf{r})d\mathbf{r} = \frac{1}{2} \int_{\Omega} (u_r(\mathbf{r}) - U_r(\mathbf{r}))\psi(\mathbf{r})d\mathbf{r}. \quad (18)$$

Here, we present two alternatives to build error estimates. The proofs of the theorems are given in the Appendix.

Theorem 1. *The error in the approximation to the solvation free energy is,*

$$\frac{1}{2} \int_{\Omega} e_r(\mathbf{r}) \psi(\mathbf{r}) d\mathbf{r} = E_{\phi} + R_{\phi} \quad (19)$$

where

$$\begin{aligned} E_{\phi} &= \frac{\epsilon_m}{2} \oint_{\Gamma} \left(\frac{\partial \phi^-}{\partial \mathbf{n}}(\mathbf{r}) u_c(\mathbf{r}) - \phi^-(\mathbf{r}) \frac{\partial u_c}{\partial \mathbf{n}}(\mathbf{r}) \right) d\mathbf{r} + \frac{\epsilon_m}{2} \oint_{\Gamma} \left(\frac{\partial \phi^-}{\partial \mathbf{n}}(\mathbf{r}) U_r^-(\mathbf{r}) - \phi^-(\mathbf{r}) \frac{\partial U_r^-}{\partial \mathbf{n}}(\mathbf{r}) \right) d\mathbf{r}, \\ R_{\phi} &= \frac{1}{2} \int_{\Omega_w \cup \Omega_m} \phi(\mathbf{r}) (-\nabla \cdot (\epsilon(\mathbf{r}) \nabla u_r(\mathbf{r})) + \bar{\kappa}^2(\mathbf{r}) u_r(\mathbf{r})) d\mathbf{r} + \frac{\epsilon_m}{2} \int_{\Omega_m} \phi(\mathbf{r}) \nabla^2 U_r(\mathbf{r}) d\mathbf{r}. \end{aligned}$$

Alternatively, we derive a different error representation.

Theorem 2. *The error in the approximation to the solvation free energy is,*

$$\frac{1}{2} \int_{\Omega} e_r(\mathbf{r}) \psi(\mathbf{r}) d\mathbf{r} = E_u + R_u \quad (20)$$

where

$$\begin{aligned} E_u &= \frac{\epsilon_m}{2} \oint_{\Gamma} \left(\frac{\partial \phi^-}{\partial \mathbf{n}}(\mathbf{r}) u_c(\mathbf{r}) - \phi^-(\mathbf{r}) \frac{\partial u_c}{\partial \mathbf{n}}(\mathbf{r}) \right) d\mathbf{r} - \frac{\epsilon_m}{2} \oint_{\Gamma} \left(u_c(\mathbf{r}) \frac{\partial U^-}{\partial \mathbf{n}}(\mathbf{r}) - \frac{\partial u_c}{\partial \mathbf{n}}(\mathbf{r}) U^-(\mathbf{r}) \right) d\mathbf{r}, \\ R_u &= \frac{1}{2} \int_{\Omega_w \cup \Omega_m} \phi(\mathbf{r}) (-\nabla \cdot (\epsilon(\mathbf{r}) \nabla u_r(\mathbf{r})) + \bar{\kappa}^2(\mathbf{r}) u_r(\mathbf{r})) d\mathbf{r}. \end{aligned}$$

Error Estimates

The error representations in equations (19) and (20) contain surface integrals (represented by E_{ϕ} and E_u) and volume integrals (represented by R_{ϕ} and R_u). In the context of BEM, evaluating volume integrals is computationally expensive. Hence, we propose the following error estimates,

$$\begin{aligned} \int_{\Omega} (u_r(\mathbf{r}) - U_r(\mathbf{r})) \psi(\mathbf{r}) d\mathbf{r} &\approx E_{\phi}, \text{ and} \\ \int_{\Omega} (u_r(\mathbf{r}) - U_r(\mathbf{r})) \psi(\mathbf{r}) d\mathbf{r} &\approx E_u, \end{aligned} \quad (21)$$

where we neglect the contributions from the volumetric terms R_{ϕ} and R_u . Our numerical results will be useful to determine if these approximations are appropriate.

Element-wise error estimation

Our aim is to find the contribution of each discretization element to the error in the numerical solution of ΔG_{solv} . To this end, we decompose the surface integrals in E_ϕ and E_u as follows,

$$\begin{aligned}
|E_\phi| &= \left| \frac{\epsilon_m}{2} \oint_{\Gamma} \left(\frac{\partial \phi^-}{\partial \mathbf{n}}(\mathbf{r}) u_c(\mathbf{r}) - \phi^-(\mathbf{r}) \frac{\partial u_c}{\partial \mathbf{n}}(\mathbf{r}) \right) d\mathbf{r} + \frac{\epsilon_m}{2} \oint_{\Gamma} \left(\frac{\partial \phi^-}{\partial \mathbf{n}}(\mathbf{r}) U_r^-(\mathbf{r}) - \phi^-(\mathbf{r}) \frac{\partial U_r^-}{\partial \mathbf{n}}(\mathbf{r}) \right) d\mathbf{r} \right|, \\
&\leq \sum_i^{N_p} \left| \frac{\epsilon_m}{2} \oint_{\Gamma_i} \left(\frac{\partial \phi^-}{\partial \mathbf{n}}(\mathbf{r}) u_c(\mathbf{r}) - \phi^-(\mathbf{r}) \frac{\partial u_c}{\partial \mathbf{n}}(\mathbf{r}) \right) d\mathbf{r} + \frac{\epsilon_m}{2} \oint_{\Gamma_i} \left(\frac{\partial \phi^-}{\partial \mathbf{n}}(\mathbf{r}) U_r^-(\mathbf{r}) - \phi^-(\mathbf{r}) \frac{\partial U_r^-}{\partial \mathbf{n}}(\mathbf{r}) \right) d\mathbf{r} \right|, \\
&= \sum_i^{N_p} E_\phi^i,
\end{aligned} \tag{22}$$

and

$$\begin{aligned}
|E_u| &= \left| \frac{\epsilon_m}{2} \oint_{\Gamma} \left(\frac{\partial \phi^-}{\partial \mathbf{n}}(\mathbf{r}) u_c(\mathbf{r}) - \phi^-(\mathbf{r}) \frac{\partial u_c}{\partial \mathbf{n}}(\mathbf{r}) \right) d\mathbf{r} - \frac{\epsilon_m}{2} \oint_{\Gamma} \left(\frac{\partial U_r^-}{\partial \mathbf{n}}(\mathbf{r}) u_c(\mathbf{r}) - U_r^-(\mathbf{r}) \frac{\partial u_c}{\partial \mathbf{n}}(\mathbf{r}) \right) d\mathbf{r} \right|, \\
&\leq \sum_i^{N_p} \left| \frac{\epsilon_m}{2} \oint_{\Gamma_i} \left(\frac{\partial \phi^-}{\partial \mathbf{n}}(\mathbf{r}) u_c(\mathbf{r}) - \phi^-(\mathbf{r}) \frac{\partial u_c}{\partial \mathbf{n}}(\mathbf{r}) \right) d\mathbf{r} - \frac{\epsilon_m}{2} \oint_{\Gamma_i} \left(\frac{\partial U_r^-}{\partial \mathbf{n}}(\mathbf{r}) u_c(\mathbf{r}) - U_r^-(\mathbf{r}) \frac{\partial u_c}{\partial \mathbf{n}}(\mathbf{r}) \right) d\mathbf{r} \right|, \\
&= \sum_i^{N_p} E_u^i,
\end{aligned} \tag{23}$$

where Γ_i corresponds to panel i in the discretization of Γ , and E_ϕ^i or E_u^i represent the contribution of element i to the error.

Numerical calculation of ϕ and U_r

The error estimates in equations (22) and (23) need the numerical approximation U_r and the adjoint ϕ , and their normal derivatives on Γ . We compute U_r using equations (8) and (9) assuming piecewise constant boundary elements. Calculating ϕ , which is in principle exact, requires more work.

Starting from the mesh where U_r is solved, we subdivide each triangular panel into four sub-triangles by placing new vertices in each edge center. We repeat this process iteratively to obtain an arbitrarily finer mesh conserving the shape of Γ . Equation (16) showed us that ϕ equals u , hence, we can also compute ϕ on Γ using equation (8), this time, on the finer mesh and using a piecewise linear ansatz. Finally, the local errors, E_ϕ^i or E_u^i , are computed

for each panel on the coarse mesh. Figure 3 is a summary of the algorithm to compute E_ϕ^i and E_u^i .

The effectivity ratio γ_{eff}

The effectivity ratio, γ_{eff} , is an indicator of the quality of the error estimation in equation (21):

$$\gamma_{eff} = \frac{E}{\Delta G_{solv} - \Delta \widehat{G}_{solv}}. \quad (24)$$

Here, ΔG_{solv} is the exact value of the solvation free energy, and E can be E_ϕ or E_u . A γ_{eff} close to 1 indicates that the error estimate is accurate. Note that ΔG_{solv} is not available for realistic molecular geometries. We compute ΔG_{solv} using Richardson extrapolation with three consecutive uniform mesh surface-conforming refinements (see figure 5), where every boundary element was divided into 4 subtriangles. Then, each refinement contains four times more elements than the previous mesh. Using those three meshes, and knowing that error scales with the average area for a piecewise constant BEM, Richardson extrapolation finds an approximation for a infinitely refined mesh^{14,48}.

Local mesh refinement

Having the contribution of each triangular element to the error, we can decide if an element should be refined. In this work, we sort the elements in descending order according to E_ϕ^i or E_u^i , and refine those that contribute most to the error, all the way until they add up to 10% of the total error ($|E_\phi|$ or $|E_u|$). Once the high-error triangles are identified, we perform a barycentric refinement into four subtriangles by adding a vertex on the midpoint of each edge. If a triangle that should not be refined shares an edge with one that was refined, this triangle is split into two, by adding an edge between the newly created vertex and the one opposite to it. However, if a triangle that should not be refined shares two edges with triangles that were refined, we use the same barycentric refinement technique on it. We can perform this procedure iteratively to obtain finer meshes. Figure 4 is a sketch of the local mesh refinement.

The *flat* mesh refinement described in figure 4 preserves the geometry of the original mesh. However, the molecular surface is smooth, and the newly created vertices should adapt to the molecular geometry to represent it more accurately. To do so, we extended the procedure from figure 4 to *conform* to the molecular geometry by using an highly refined mesh in the background, and rather than adding the vertex in the edge midpoint, we add the closest vertex of the background mesh. This way, we make sure the vertex is on the molecular surface. This process, however, may generate elongated elements, which affect the matrix condition and quality of the solution. Then, we use the *ImproveSurfMesh* script from GAMer⁴⁹, which improves the mesh of the molecular surface preserving its geometry. We call this extended scheme *surface-conforming refinement*, and is summarized in figure 5.

RESULTS AND DISCUSSION

In this section, we start by assessing the accuracy of the estimators E_ϕ and E_u on methanol, to then use them in an adaptive mesh refinement scheme on a spherical molecule. We then apply this method on realistic molecular geometries, in particular, methanol and arginine. First, we use methanol to find optimal meshes for the calculation of ϕ , and then adaptively refine a mesh on arginine to analyze the effectiveness of the algorithm.

Accuracy of the estimators E_ϕ and E_u .

We first assessed the performance of the error estimators E_ϕ and E_u using the effectivity ratio γ_{eff} . The results in Table 1 show γ_{eff} for methanol using a mesh with 0.5 and 1 elements per Å². The adjoint ϕ was computed on a finer mesh with N_ϕ elements, obtained by flat-refining all elements of the original mesh into four subtriangles recursively (see figure 5).

We expect that a good error estimator would yield $\gamma_{eff} \approx 1$. In table 1, we see that as ϕ is computed accurately (higher N_ϕ), γ_{eff} does approach 1 for E_u , but not for E_ϕ . This is an indication that the approximation of setting $R_\phi = 0$ in theorem 1 is not accurate, and the volumetric integral term has a large contribution. Regardless, we continued studying the

performance of E_ϕ as a per-element error indicator for adaptive mesh refinement.

The detailed distributions of the per-element error estimates are presented in figures 6 and 7. It is interesting to note that the error maps for E_u and E_ϕ look almost identical, indicating that they estimate the per-element error distribution similarly, and they recognize the same high-error elements, despite a poor γ_{eff} for E_ϕ .

Mesh refinement on a spherical molecule

Even though a spherical cavity with internal charges may not be relevant physically, this test becomes useful to understand how the error is distributed on the mesh, as we can control the charge locations, and its effect on the solvation energy, since it has an analytical solution. Here, we analyzed the error distribution for two configurations, according to figure 8: a single off-centered point charge located at half the radius, and a charge and dipole (created by two point charges) placed opposite to each other, 0.62 into the radius (figure). For each case, we performed 20 recursive iterations of the surface-conforming adaptive mesh refinement scheme in figure 5. The adjoint ϕ was computed on a uniformly flat refined mesh, where every triangle was divided once into four subtriangles.

Figures 9 and 10 show $\Delta\hat{G}_{solv}$ and error with respect to an analytical solution ($\Delta G_{solv} = -52.462648$ kcal/mol and $\Delta G_{solv} = -65.467255$ kcal/mol for the Off-centered and Charge-dipole respectively)⁵⁰, computed with the meshes generated from our adaptive mesh refinement scheme. The red crosses and black triangles correspond to results with meshes generated using E_u and E_ϕ , respectively, and they have similar behavior approaching the analytical solution (black segmented line). This is an indication that in the context of solvation energy, both estimators are equivalent. The grey dotted lines are the results using a uniformly refined mesh (all elements refined with a surface-conforming method). The fact that the red crosses and black triangles are consistently closer to the analytical solution compared to the grey line is evidence of the effectivity of the adaptive mesh refinement. This is further supported by figures 9 and 10, that evidence a linear relation between the error and number of elements, which is the expected behavior of a piecewise constant BEM¹⁴.

Figure 11 shows the initial mesh, and the resulting meshes after performing the adaptive

refinement scheme iteratively 10, 15, and 20 times, with the corresponding per-element error estimation. As one could expect, it is evident that refinement is more intense closer to the charge (top of the sphere), and that the bottom of the sphere is more refined for the charge-dipole configuration, compared to the offcentered charge. Moreover, the resulting mesh of the charge-dipole case has more elements near the charge than near the dipole, showing that the charge has a higher influence in the error. Comparing the error distribution on the final mesh between E_ϕ and E_u , we see that the error is lower and more homogeneously distributed for E_ϕ . This is a surprising fact, considering E_ϕ has a worse γ_{eff} compared to E_u .

Adaptive mesh refinement for realistic molecular geometries

In this section, we study the behavior of our adaptive mesh refinement method on molecular geometries, in particular, for methanol and arginine. These results are useful to determine the impact of this scheme in real applications.

Accuracy of the adjoint

As a first study of our mesh refinement scheme for realistic molecular geometries, we look at the influence of the accuracy in the calculation of ϕ on the resulting meshes. Our aim is to determine how fine of a mesh for ϕ is required for it to be effective in an adaptive refinement setting. Moreover, the calculation of ϕ represents the most time consuming part of the algorithm, which may be mitigated by using a coarse mesh. Starting from meshes of the molecular surface of methanol with 0.5 and 1 elements per \AA^2 , we applied the adaptive mesh refinement technique iteratively 6 times, using the surface-conforming scheme. We computed ϕ in two ways: (a) on the same mesh as U_r (*coarse*), and (b) on a mesh with 64 times more elements (*fine*), obtained by flat refining all triangles recursively 3 times. Figure 12 shows $\Delta\hat{G}_{solv}$ and the error with respect to a Richardson extrapolated value, where the red and black lines use the coarse and fine meshes for ϕ , respectively. The results with the fine and coarse meshes are very similar, which is evidence that the accuracy of the adjoint has a weak effect on the adaptive mesh refinement, and computing ϕ on the same mesh as U_r is sufficient.

We also present more fine-grained comparisons in figures 13 and 14, where the element-wise error (E_u) and electrostatic potential are plotted, respectively, on the original mesh and after 2, 4, and 6 iterations of the adaptive mesh refinement. We did not include the equivalent result to figure 13 for E_ϕ to avoid redundancy, as it was very similar. From these plots, we can see that the resulting meshes with a coarse and fine calculation of ϕ are different, even though they yield similar $\Delta\hat{G}_{solv}$. This happens because even with a poor approximation of ϕ , the error estimate E_u is capable of detecting high error elements appropriately. Moreover, we can see from the results in figure 14 that regions with high electrostatic potential coincide with large error panels (figure 13), and our adaptive mesh refinement technique adds more elements in that area.

Mesh refinement on larger structures

To estimate the error in larger molecules using a very fine mesh for ϕ would be time consuming, however, the results in figure 12 indicate that we can compute it on the same mesh as U_r . Here, we use this fact to perform an adaptive mesh refinement on arginine, starting from meshes with 0.5, 1, and 2 elements per \AA^2 , aiming towards finding an optimal mesh to compute the solvation energy.

Figure 15 shows the convergence of the solvation energy as we apply the adaptive mesh refinement iteratively, using E_ϕ and E_u . We can see that both error estimates generate meshes that are approaching an exact value (obtained with Richardson extrapolation), however, E_u slightly outperforms E_ϕ . The effectiveness of the adaptive mesh refinement becomes evident as, for example, using a mesh refined adaptively from 0.5 elements per \AA^2 can reach an error that is lower than the calculation with 2 elements per \AA^2 , with near half the number of elements.

We can find further evidence of the power of the mesh refinement technique in figure 16. Those plots show the relative error in the x axis and time to solution in the y axis for runs performed with each mesh of the adaptive mesh refinement process, using E_u (red) and E_ϕ (black). The size of the markers correspond to the number of elements, and their color to the number of GMRES iterations. Note that the large number of iterations is due to a tight GMRES tolerance (10^{-8}), and the fact we use an integral formulation that yields an

ill-conditioned matrix, without a preconditioner. We can see that as we refine the mesh, the number of elements grows slightly (symbols’ sizes remain similar), however, the error drops significantly. For example, performing six iterations of the adaptive mesh refinement scheme on the mesh with 0.5 elements per \AA^2 , the element count only increases from 282 to 328 ($\sim 16\%$), whereas the error decreases one order of magnitude. This same behavior is present in the tests starting from 1 and 2 elements per \AA^2 . While the number of elements only increases mildly with adaptive refinement, the computer time increases somewhat, as shown by the rightmost plot in figure 16. This is because the computer time in these simulations is dominated by the number of iterations rather than the mesh size (see that the simulations that took longer have consistently lighter symbols). This computer time would decrease if we used better conditioned integral formulations¹⁷ or preconditioners⁵¹, which control the iteration count. Also, these plots show that the meshes generated with E_u (red line) tend to outperform those generated with E_ϕ (black line), as the red line is mostly underneath the black line.

CONCLUSIONS

This work presents two adjoint-based goal-oriented error estimates, E_ϕ and E_u , for the Poisson-Boltzmann equation with BEM, where the quantity of interest is the solvation energy of a solute molecule. These estimates are written in such a way that we can compute the contribution of each discretization element to the total error, which is useful to detect high-error panels of the mesh. We saw that even though E_u predicts the error better than E_ϕ (γ_{eff} closer to 1), both estimates detect the same high-error areas of the mesh.

We used these per-element error indicators to build an adaptive mesh refinement technique, which we tested on a spherical molecule, methanol, and arginine. Both error estimators had a similar performance in the adaptive mesh refinement, and we found that errors tend to concentrate in areas with high electrostatic potential. Also, we realized that the accuracy in the calculation of the adjoint had a weak effect on the resulting mesh from the adaptive refinement, and we did not require a finer mesh to resolve it. We showcase the power of the adaptive mesh refinement in the results for arginine, where the error dropped

a factor of 10, by increasing the number of elements only 16%.

As future work, we plan to use the adaptive mesh refinement technique to generate optimal meshes automatically, aiming towards computing the solvation energy in large-scale molecular simulations efficiently⁵².

SUPPORTING INFORMATION

All data and code to reproduce the results of this paper can be obtained from the Github repository <https://github.com/RammVI/Error-Formulation>.

ACKNOWLEDGMENTS

The authors thank Michael Karkulik (USM) and Ignacio Muga (PUCV) for very helpful conversations. C. Cooper and V. Ramm acknowledge the financial support from ANID (Chile) through FONDECYT Iniciación 11160768. C. Cooper is also funded by ANID through Basal FB0821. J. Chaudhry's work is supported by the NSF-DMS (USA) 1720402.

APPENDIX

Proof of theorem 1

Proof. Using (16),

$$\frac{1}{2} \int_{\Omega} e_r(\mathbf{r}) \psi(\mathbf{r}) d\mathbf{r} = \frac{1}{2} \int_{\Omega} (u_r(\mathbf{r}) - U_r(\mathbf{r})) (-\nabla \cdot (\epsilon(\mathbf{r}) \nabla \phi(\mathbf{r})) + \bar{\kappa}^2(\mathbf{r}) \phi(\mathbf{r})) d\mathbf{r}, \quad (25)$$

$$\begin{aligned} &= \frac{1}{2} \int_{\Omega} u_r(\mathbf{r}) (-\nabla \cdot (\epsilon(\mathbf{r}) \nabla \phi(\mathbf{r})) + \bar{\kappa}^2(\mathbf{r}) \phi(\mathbf{r})) d\mathbf{r}, \\ &- \frac{1}{2} \int_{\Omega} U_r(\mathbf{r}) (-\nabla \cdot (\epsilon(\mathbf{r}) \nabla \phi(\mathbf{r})) + \bar{\kappa}^2(\mathbf{r}) \phi(\mathbf{r})) d\mathbf{r}, = I - II \end{aligned} \quad (26)$$

where

$$I = \frac{1}{2} \int_{\Omega} u_r(\mathbf{r}) (-\nabla \cdot (\epsilon(\mathbf{r}) \nabla \phi(\mathbf{r})) + \bar{\kappa}^2(\mathbf{r}) \phi(\mathbf{r})) d\mathbf{r} \quad (27)$$

$$II = \frac{1}{2} \int_{\Omega} U_r(\mathbf{r}) (-\nabla \cdot (\epsilon(\mathbf{r}) \nabla \phi(\mathbf{r})) + \bar{\kappa}^2(\mathbf{r}) \phi(\mathbf{r})) d\mathbf{r}. \quad (28)$$

First we consider the term I .

$$\begin{aligned} I &= \frac{1}{2} \int_{\Omega} [-\nabla \cdot (\epsilon(\mathbf{r}) \nabla \phi(\mathbf{r})) + \bar{\kappa}^2 \phi(\mathbf{r})] u_r(\mathbf{r}) d\mathbf{r}, \\ &= \frac{1}{2} \left[\int_{\Omega_m} -\epsilon_m \nabla^2 \phi(\mathbf{r}) u_r(\mathbf{r}) d\mathbf{r} + \int_{\Omega_w} -\epsilon_s \nabla^2 \phi(\mathbf{r}) u_r(\mathbf{r}) d\mathbf{r} + \int_{\Omega_w} \bar{\kappa}^2 \phi(\mathbf{r}) u_r(\mathbf{r}) d\mathbf{r} \right]. \end{aligned} \quad (29)$$

We now use separation of variables to write

$$\begin{aligned} I &= \frac{1}{2} \left[- \int_{\Omega_m} \{ \epsilon_m \nabla \cdot (\nabla \phi(\mathbf{r}) u_r(\mathbf{r})) - \epsilon_m \nabla \cdot (\phi(\mathbf{r}) \nabla u_r(\mathbf{r})) + \phi(\mathbf{r}) (\epsilon_m \nabla^2 u_r(\mathbf{r})) \} d\mathbf{r} \right. \\ &\quad - \int_{\Omega_w} \{ \epsilon_w \nabla \cdot (\nabla \phi(\mathbf{r}) u_r(\mathbf{r})) - \epsilon_w \nabla \cdot (\phi(\mathbf{r}) \nabla u_r(\mathbf{r})) + \phi(\mathbf{r}) (\epsilon_w \nabla^2 u_r(\mathbf{r})) \} d\mathbf{r} \\ &\quad \left. + \int_{\Omega_w} \phi(\mathbf{r}) \bar{\kappa}^2 u_r(\mathbf{r}) d\mathbf{r} \right] \end{aligned} \quad (30)$$

and then use the divergence theorem to obtain

$$\begin{aligned} I &= \frac{1}{2} \left[- \oint_{\Gamma} \left(\epsilon_m \frac{\partial \phi^-}{\partial \mathbf{n}}(\mathbf{r}) u_r^-(\mathbf{r}) - \phi^-(\mathbf{r}) \epsilon_m \frac{\partial u_r^-}{\partial \mathbf{n}}(\mathbf{r}) - \epsilon_w \frac{\partial \phi^+}{\partial \mathbf{n}}(\mathbf{r}) u_r^+(\mathbf{r}) + \phi^+(\mathbf{r}) \epsilon_w \frac{\partial u_r^+}{\partial \mathbf{n}}(\mathbf{r}) \right) d\mathbf{r} \right. \\ &\quad \left. + \int_{\Omega_w + \Omega_m} \phi(\mathbf{r}) (-\nabla \cdot (\epsilon(\mathbf{r}) \nabla u_r(\mathbf{r})) + \bar{\kappa}^2(\mathbf{r}) u_r(\mathbf{r})) d\mathbf{r} \right], \end{aligned} \quad (31)$$

recalling that \mathbf{n} points out of Ω_m . Then, we can apply the interface conditions on ϕ (equation (17)) and u_r (equation (6)) to write

$$\begin{aligned} I &= \frac{\epsilon_m}{2} \oint_{\Gamma} \left(\frac{\partial \phi^-}{\partial \mathbf{n}}(\mathbf{r}) u_c(\mathbf{r}) - \phi^-(\mathbf{r}) \frac{\partial u_c}{\partial \mathbf{n}}(\mathbf{r}) \right) d\mathbf{r} \\ &\quad + \frac{1}{2} \int_{\Omega_w + \Omega_m} \phi(\mathbf{r}) (-\nabla \cdot (\epsilon(\mathbf{r}) \nabla u_r(\mathbf{r})) + \bar{\kappa}^2(\mathbf{r}) u_r(\mathbf{r})) d\mathbf{r}. \end{aligned} \quad (32)$$

Now, considering the term II in equation (),

$$\begin{aligned} II &= \frac{1}{2} \int_{\Omega} \left[\sum_k^{N_q} q_k \delta(\mathbf{r} - \mathbf{r}_k) \right] U_r(\mathbf{r}) d\mathbf{r}, \\ &= \frac{1}{2} \int_{\Omega} [-\nabla \cdot (\epsilon(\mathbf{r}) \nabla \phi(\mathbf{r})) + \bar{\kappa}^2 \phi(\mathbf{r})] U_r(\mathbf{r}) d\mathbf{r}, \\ &= \frac{1}{2} \int_{\Omega_m} -\epsilon_m \nabla^2 \phi(\mathbf{r}) U_r(\mathbf{r}) d\mathbf{r} + \frac{1}{2} \int_{\Omega_w} [-\epsilon_s \nabla^2 \phi(\mathbf{r}) + \bar{\kappa}^2 \phi(\mathbf{r})] U_r(\mathbf{r}) d\mathbf{r}. \end{aligned} \quad (33)$$

Considering that there are no point charges in the outer region, equation (16) equals zero in Ω_w , and the last integral equation (33) cancels out. Using separation of variables and the divergence theorem, we can write

$$\begin{aligned}
II &= -\frac{\epsilon_m}{2} \int_{\Omega_m} \nabla^2 \phi(\mathbf{r}) U_r(\mathbf{r}) d\mathbf{r}, \\
&= -\frac{\epsilon_m}{2} \int_{\Omega_m} [\nabla \cdot (\nabla \phi(\mathbf{r}) U_r(\mathbf{r})) - \nabla \cdot (\phi(\mathbf{r}) \nabla U_r(\mathbf{r})) + \phi(\mathbf{r}) \nabla^2 U_r(\mathbf{r})] d\mathbf{r}, \\
&= -\frac{\epsilon_m}{2} \left[\oint_{\Gamma} \left(\frac{\partial \phi^-}{\partial \mathbf{n}}(\mathbf{r}) U_r^-(\mathbf{r}) - \phi^-(\mathbf{r}) \frac{\partial U_r^-}{\partial \mathbf{n}}(\mathbf{r}) \right) d\mathbf{r} + \int_{\Omega_m} \phi(\mathbf{r}) \nabla^2 U_r(\mathbf{r}) d\mathbf{r} \right]. \quad (34)
\end{aligned}$$

Combining equations (26), (32) and (34) completes the proof. \square

Proof of theorem 2

Proof. We start from equation (18), to decompose the error as

$$\frac{1}{2} \int_{\Omega} (u_r(\mathbf{r}) - U_r(\mathbf{r})) \psi d\mathbf{r} = \frac{1}{2} \int_{\Omega} u_r(\mathbf{r}) \psi d\mathbf{r} - \frac{1}{2} \int_{\Omega} U_r(\mathbf{r}) \psi d\mathbf{r} = I - II, \quad (35)$$

where

$$I = \frac{1}{2} \int_{\Omega} u_r(\mathbf{r}) \psi d\mathbf{r} = \frac{1}{2} \int_{\Omega} [-\nabla \cdot (\epsilon(\mathbf{r}) \nabla \phi(\mathbf{r})) + \bar{\kappa}^2 \phi(\mathbf{r})] u_r(\mathbf{r}) d\mathbf{r}, \quad (36)$$

$$II = \frac{1}{2} \int_{\Omega} U_r(\mathbf{r}) \psi d\mathbf{r}. \quad (37)$$

We already derived an expression for term I in equation (32), and we will move straight to term II . Using equation (13) and considering $\psi = \rho = \sum_{k=1}^{N_q} q_k \delta(|\mathbf{r} - \mathbf{r}_k|)$ in equation (1), we find

$$II = \frac{1}{2} \int_{\Omega} U_r(\mathbf{r}) \sum_{k=1}^{N_q} q_k \delta(|\mathbf{r} - \mathbf{r}_k|) d\mathbf{r} = \frac{1}{2} \sum_{k=1}^{N_q} U_r(\mathbf{r}_k) q_k. \quad (38)$$

U_r can be further expanded with the numerical approximation of equation (9) to write

$$II = \frac{1}{2} \sum_{k=1}^{N_q} q_k \left[- \oint_{\Gamma} U^-(\mathbf{r}) \frac{\partial}{\partial \mathbf{n}} \left(\frac{1}{4\pi |\mathbf{r}_k - \mathbf{r}|} \right) d\mathbf{r} + \oint_{\Gamma} \frac{\partial U^-(\mathbf{r})}{\partial \mathbf{n}} \frac{1}{4\pi |\mathbf{r}_k - \mathbf{r}|} d\mathbf{r} \right]. \quad (39)$$

Considering the sum and integral are linear operators, we can swap them to bring $\sum_{k=1}^{N_k} q_k$ into the integral, as

$$II = \frac{1}{2} \left[- \oint_{\Gamma} U^-(\mathbf{r}) \frac{\partial}{\partial \mathbf{n}} \underbrace{\left(\sum_{k=1}^{N_q} q_k \frac{1}{4\pi |\mathbf{r}_k - \mathbf{r}|} \right)}_{=\epsilon_m u_c} d\mathbf{r} + \oint_{\Gamma} \frac{\partial U^-(\mathbf{r})}{\partial \mathbf{n}} \underbrace{\sum_{k=1}^{N_q} q_k \frac{1}{4\pi |\mathbf{r}_k - \mathbf{r}|}}_{=\epsilon_m u_c} d\mathbf{r} \right], \quad (40)$$

where, as indicated in the previous equation, we have recovered u_c from equation (4). Then, we get

$$II = \frac{\epsilon_m}{2} \left[- \oint_{\Gamma} U^-(\mathbf{r}) \frac{\partial u_c}{\partial \mathbf{n}}(\mathbf{r}) d\mathbf{r} + \oint_{\Gamma} \frac{\partial U^-(\mathbf{r})}{\partial \mathbf{n}} u_c(\mathbf{r}) d\mathbf{r} \right]. \quad (41)$$

Combining equations (35), (32) and (41) completes the proof.

□

Figure 1: (Left) Solute molecule surrounded by explicit solvent molecules. (Right) Representation of the implicit solvent model. The hatched area corresponds to the unbounded implicit solvent (Ω_w , with ϵ_w and κ), which has a cavity containing the solute molecule (Ω_m , with ϵ_m).

Figure 2: Thermodynamic cycle of molecular solvation. Initially (pane I), the solute is isolated in vacuum (only point charges) and the electrostatic potential in the solvent is zero. Then, we place the charges inside the solvent, generating a reaction potential (pane II).

Figure 3: Process of creating the mesh, solving and calculating the error.

Figure 4: Example of a local mesh refinement procedure. In the left pane, the two elements marked in blue are identified to have a high E_ϕ^i or E_u^i , and will be subdivided into four triangles. In the middle pane we identify neighbor elements: those marked in light blue only share one edge with the high-error triangles, and they will be divided in two, however, there is one triangle in the middle that shares two edges with refined triangles, then, we mark it in blue, and it will be refined in four triangles. This generates a new neighbor triangle to be divided in two, marked in light blue below the blue triangles. Finally, the right pane shows the resulting refined mesh. We can perform this procedure iteratively for higher mesh refinements.

Figure 5: Summary of the local mesh refinement procedure.

Figure 6: Per-element error estimation for methanol with a $0.5 \text{ el}/\text{\AA}^2$ mesh.

Figure 7: Per-element error estimation for methanol with a $1 \text{ el}/\text{\AA}^2$ mesh.

Figure 8: Offcenter charge (top) and charge-dipole (bottom) distributions for the spherical cavity

Figure 9: Solvation energy (left) and error (right) for the off-centered charge configuration. Meshes for the results marked with red crosses were obtained with E_u ($\Delta\hat{G}_{solv}^u$) and the ones marked with black triangles were obtained with E_ϕ ($\Delta\hat{G}_{solv}^\phi$). The grey dotted lines correspond to uniformly refined meshes (all elements with a surface conforming method, $\Delta\hat{G}_{solv}^{unif}$). The segmented black line is the true solution (ΔG_{solv}), computed analytically.

Figure 10: Solvation energy (left) and error (right) for the charge-dipole configuration. Meshes for the results marked with red crosses were obtained with E_u ($\Delta\hat{G}_{solv}^u$) and the ones marked with black triangles were obtained with E_ϕ ($\Delta\hat{G}_{solv}^\phi$). The grey dotted lines correspond to uniformly refined meshes (all elements with a surface conforming method, $\Delta\hat{G}_{solv}^{unif}$). The segmented black line is the true solution (ΔG_{solv}), computed analytically.

Figure 11: Initial and resulting meshes after 10, 15, and 20 adaptive refinements for the sphere cases. Colors correspond to the per-element error estimations E_ϕ and E_u .

Figure 12: Solvation energy (top) and error (bottom) for methanol with meshes refined adaptively, computing ϕ on a coarse (red line) and fine (black line) mesh, starting from a mesh with $0.5[El/\text{\AA}^2]$ (left) and $1.0[El/\text{\AA}^2]$ (right). Solid lines correspond to results using E_u , whereas segmented lines used E_ϕ .

Figure 13: Per element error estimation (E_u^i) using a *fine* and *coarse* mesh to obtain ϕ .

Figure 14: Total electrostatic potential on the molecular surface.

Figure 15: $\Delta\hat{G}_{solv}$ (left) and error (right) for arginine using meshes generated with the adaptive mesh refinement technique with a surface-conforming scheme. Results in red use E_u ($\Delta\hat{G}_{solv}^u$) whereas those in black use E_ϕ ($\Delta\hat{G}_{solv}^\phi$). The black segmented line in the left pane corresponds to a Richardson extrapolated value for the energy, which is also used as the reference for the error calculations.

Figure 16: Relative error versus time to solution for each mesh using adaptive refinement. Size and color of the markers indicate the number of mesh elements and number of GMRES iterations, respectively. Results following the red line use E_u whereas those following the black line use E_ϕ .

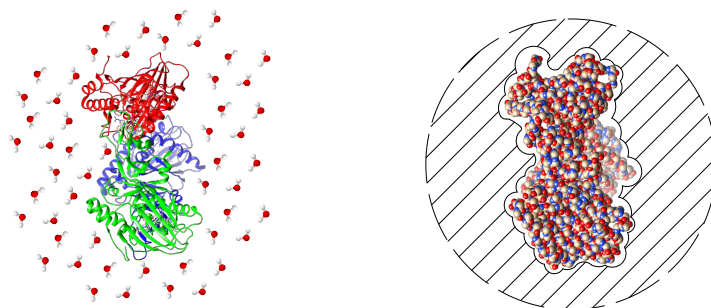


Figure 1
Vicente Ramm, Jehanzeb H.
Chaudhry, Christopher D.
Cooper
J. Comput. Chem.

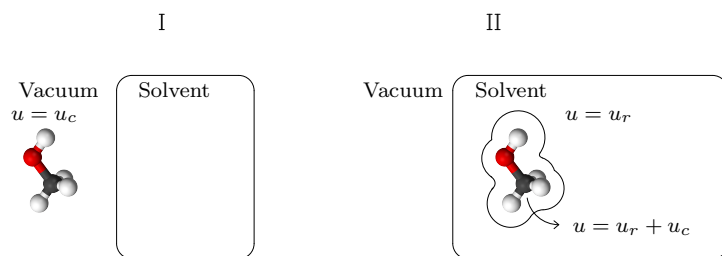


Figure 2
 Vicente Ramm, Jehanzeb H.
 Chaudhry, Christopher D.
 Cooper
 J. Comput. Chem.

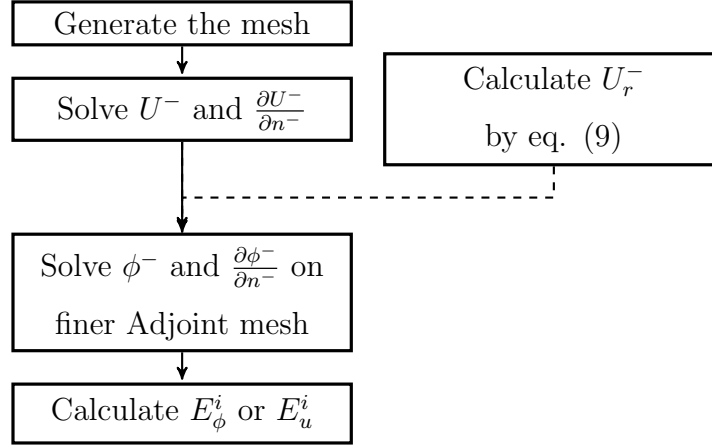


Figure 3
 Vicente Ramm, Jehanzeb H.
 Chaudhry, Christopher D.
 Cooper
 J. Comput. Chem.

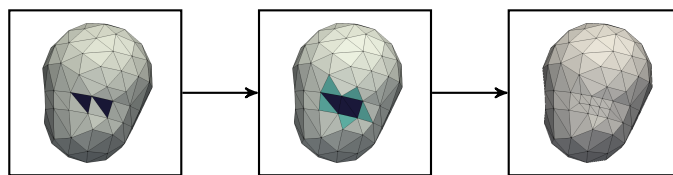


Figure 4
Vicente Ramm, Jehanzeb H.
Chaudhry, Christopher D.
Cooper
J. Comput. Chem.

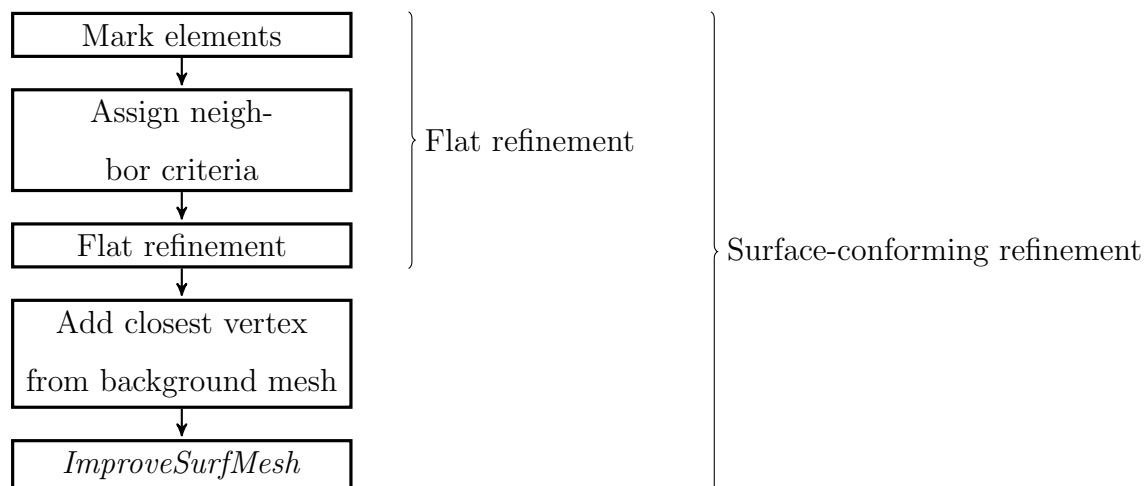


Figure 5
 Vicente Ramm, Jehanzeb H.
 Chaudhry, Christopher D.
 Cooper
 J. Comput. Chem.

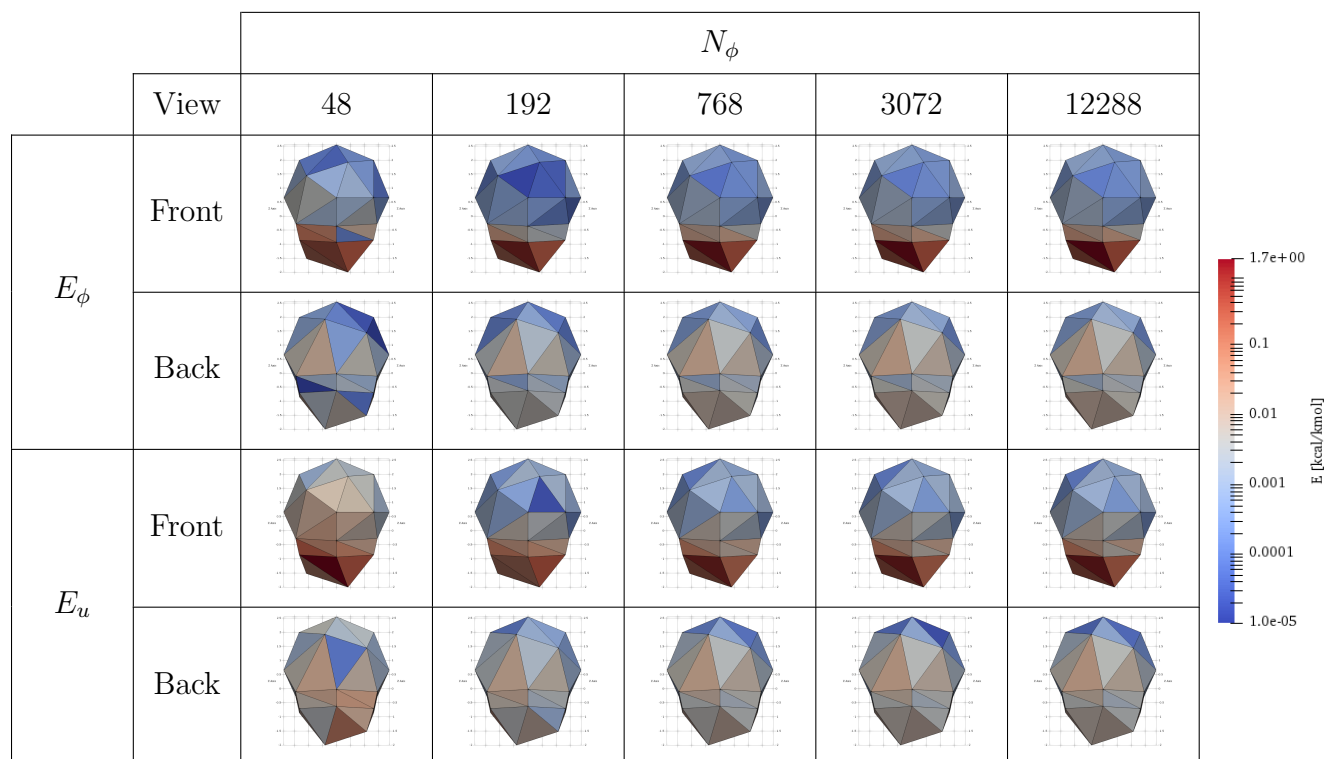


Figure 6
 Vicente Ramm, Jehanzeb H.
 Chaudhry, Christopher D.
 Cooper
 J. Comput. Chem.

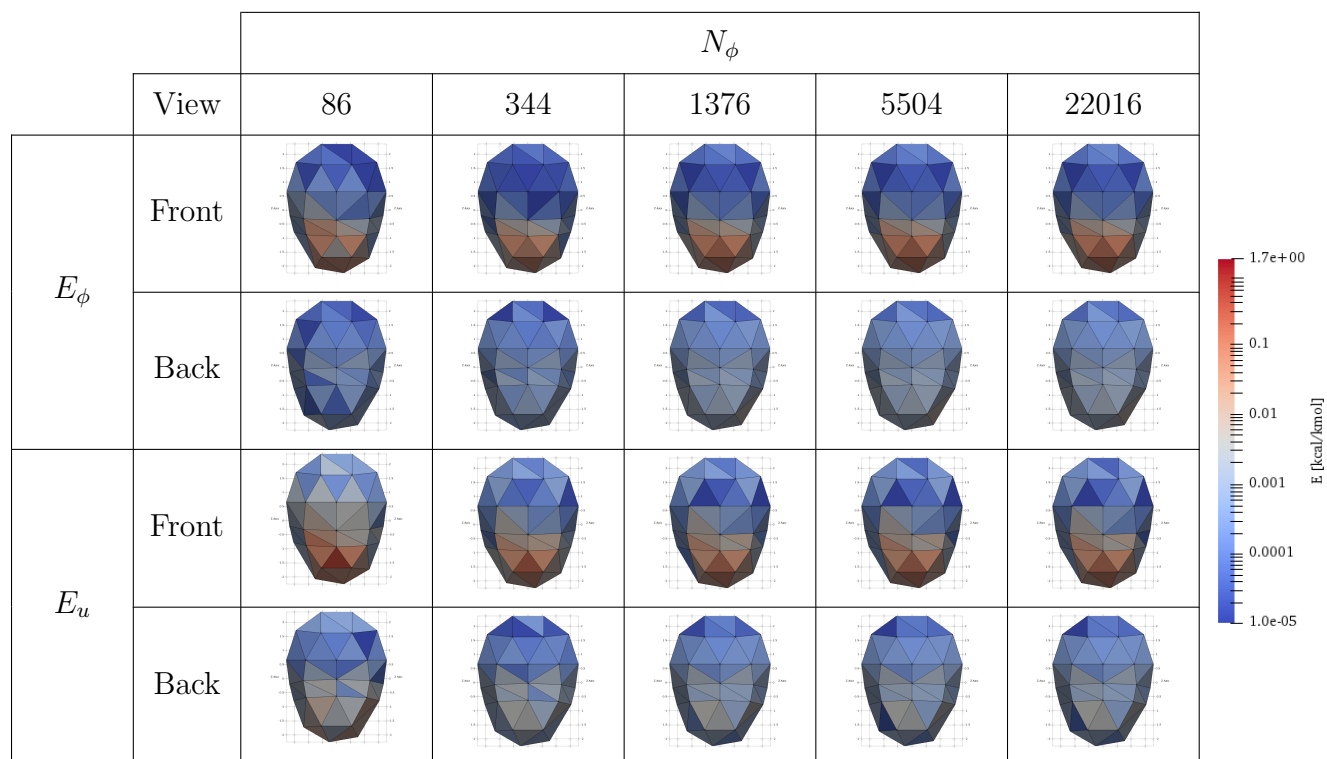


Figure 7
 Vicente Ramm, Jehanzeb H.
 Chaudhry, Christopher D.
 Cooper
 J. Comput. Chem.

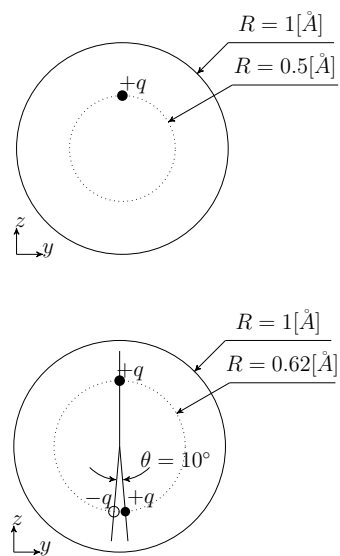


Figure 8
 Vicente Ramm, Jehanzeb H.
 Chaudhry, Christopher D.
 Cooper
 J. Comput. Chem.

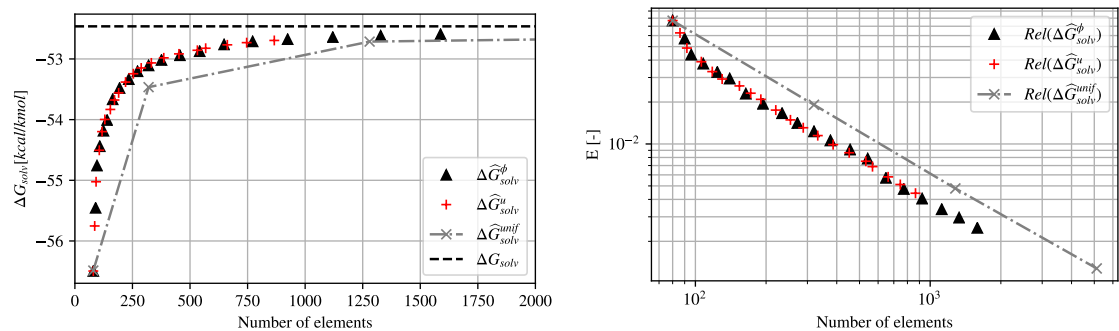


Figure 9
 Vicente Ramm, Jehanzeb H.
 Chaudhry, Christopher D.
 Cooper
 J. Comput. Chem.

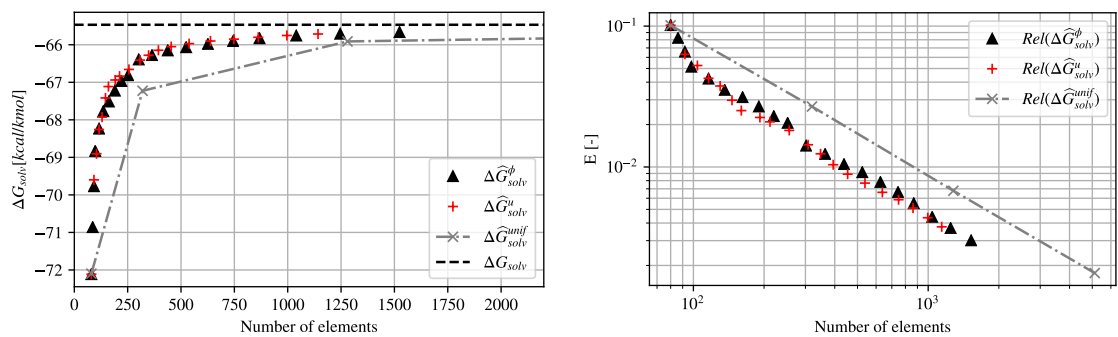


Figure 10
 Vicente Ramm, Jehanzeb H.
 Chaudhry, Christopher D.
 Cooper
 J. Comput. Chem.

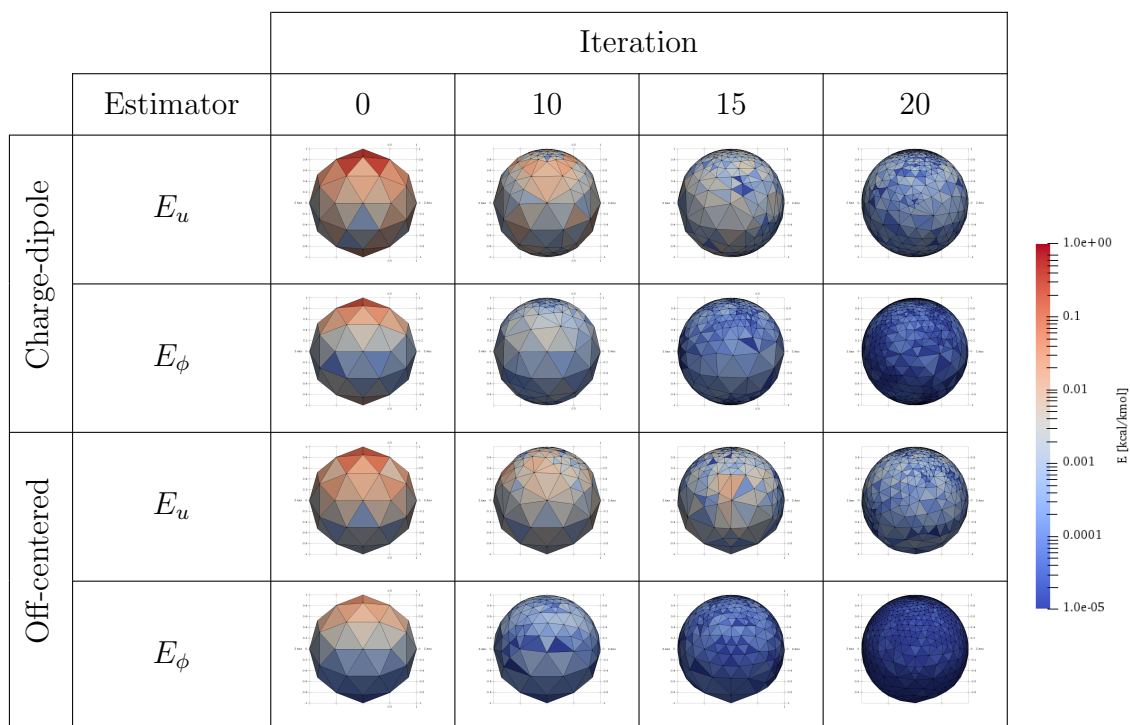


Figure 11
 Vicente Ramm, Jehanzeb H.
 Chaudhry, Christopher D.
 Cooper
 J. Comput. Chem.

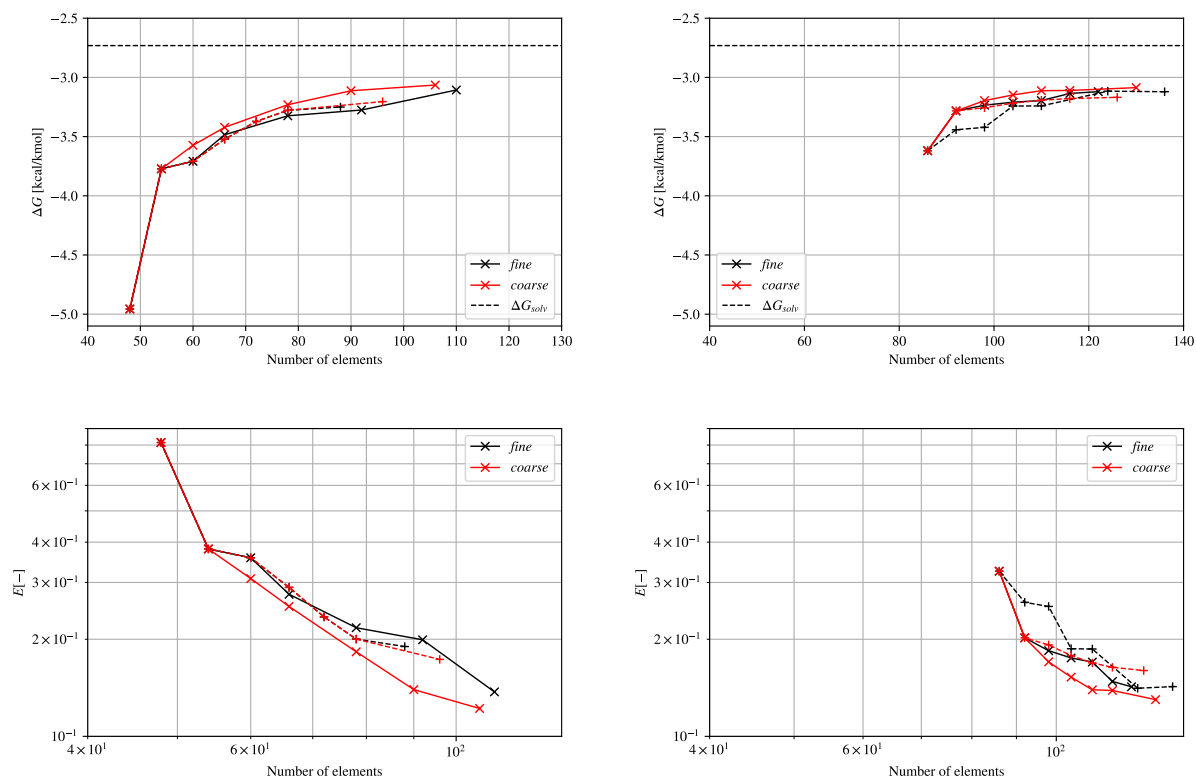


Figure 12
 Vicente Ramm, Jehanzeb H.
 Chaudhry, Christopher D.
 Cooper
 J. Comput. Chem.

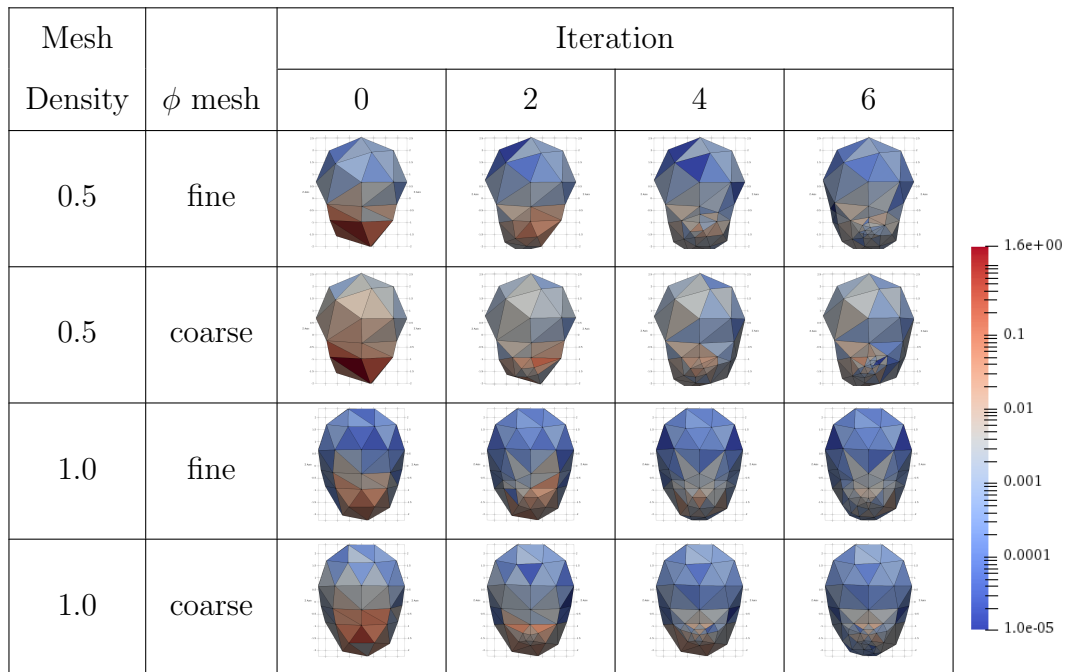


Figure 13
 Vicente Ramm, Jehanzeb H.
 Chaudhry, Christopher D.
 Cooper
 J. Comput. Chem.

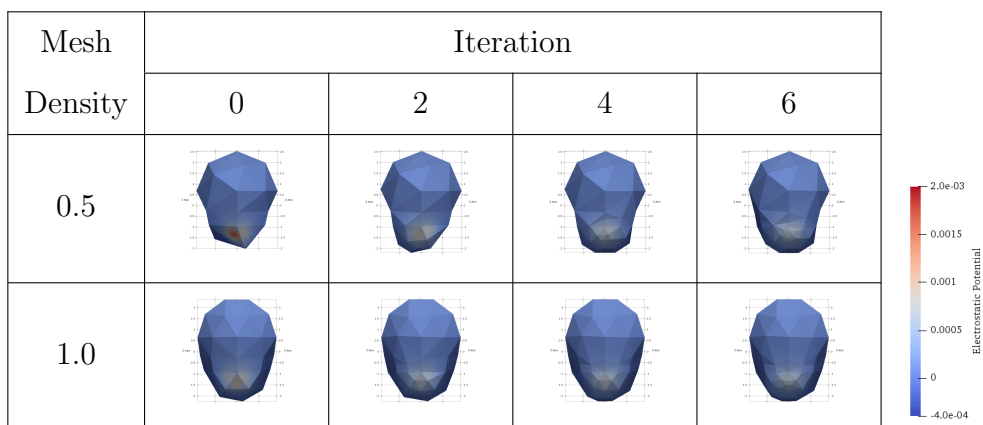


Figure 14
 Vicente Ramm, Jehanzeb H.
 Chaudhry, Christopher D.
 Cooper
 J. Comput. Chem.

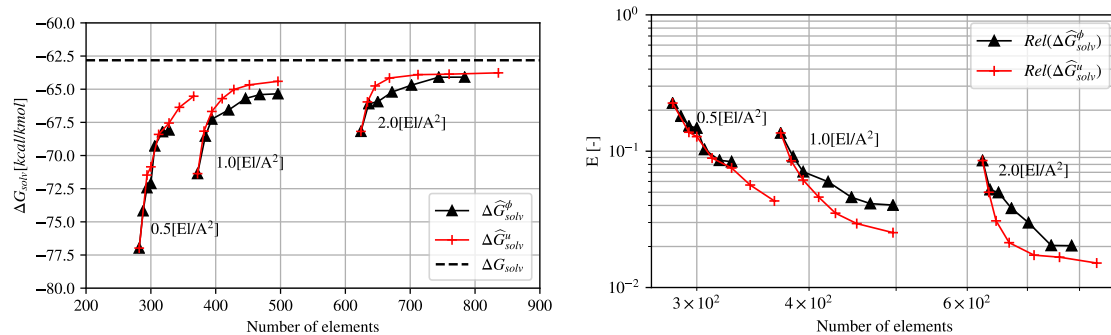


Figure 15
 Vicente Ramm, Jehanzeb H.
 Chaudhry, Christopher D.
 Cooper
 J. Comput. Chem.

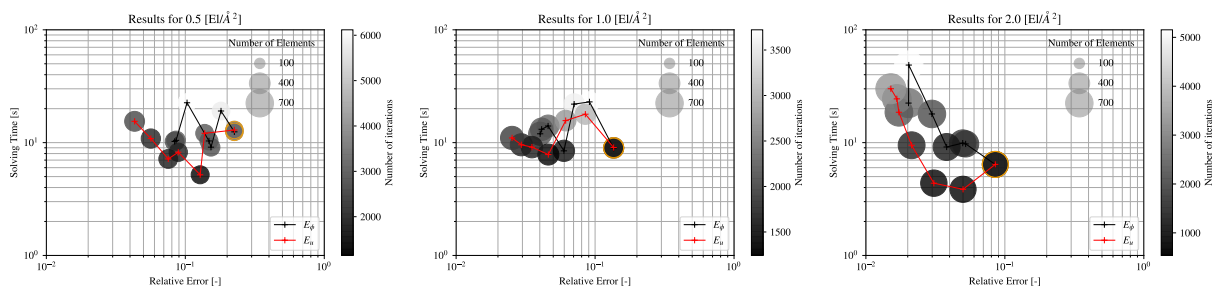


Figure 16
 Vicente Ramm, Jehanzeb H.
 Chaudhry, Christopher D.
 Cooper
 J. Comput. Chem.

Density	N_ϕ	E_ϕ	γ_{eff}^ϕ	E_u	γ_{eff}^u
0.5	48	0.1461	-0.089	1.5774	-0.963
	192	-1.2512	0.764	-0.4864	0.297
	768	-1.9297	1.178	-1.2182	0.744
	3072	-2.2426	1.369	-1.4882	0.908
	12288	-2.3300	1.422	-1.5668	0.956
$\Delta\hat{G}_{solv} = -4,9431$ kcal/mol			$\Delta G_{solv} = -6,5815$ kcal/mol		
1.0	86	0.0138	0.012	0.4806	-2.501
	344	-0.2841	-0.241	-0.0217	0.113
	1376	-0.4393	-0.373	-0.1481	0.771
	5504	-0.4856	-0.412	-0.1815	0.944
	22016	-0.4980	-0.423	-0.1906	0.992
$\Delta\hat{G}_{solv} = -3,5731$ kcal/mol			$\Delta G_{solv} = -3,7652$ kcal/mol		

Table 1: γ_{eff} for methanol with 0.5 and 1 elements per Å². N_ϕ is the number of elements in the mesh to compute ϕ .

References

1. B. Roux and T. Simonson, Biophys. Chem. **78**, 1 (1999).
2. N. A. Baker, Meth. Enzymol. **383**, 94 (2004).
3. R. C. Harris, A. H. Boschitsch, and M. O. Fenley, Journal of chemical theory and computation **9**, 3677 (2013).
4. M. L. Connolly, J. Appl. Cryst. **16**, 548 (1983).
5. B. Honig and A. Nicholls, Science **268**, 1144 (1995).
6. N. A. Baker, D. Sept, M. J. Holst, and J. A. McCammon, P. Natl. Acad. Sci. USA **98**, 10037 (2001).
7. D. Chen, Z. Chen, C. Chen, W. Geng, and G.-W. Wei, Journal of computational chemistry **32**, 756 (2011).

8. M. Holst, N. Baker, and F. Wang, *Journal of computational chemistry* **21**, 1319 (2000).
9. N. Baker, M. Holst, and F. Wang, *Journal of computational chemistry* **21**, 1343 (2000).
10. S. D. Bond, J. H. Chaudhry, E. C. Cyr, and L. N. Olson, *Journal of computational chemistry* **31**, 1625 (2010).
11. B. Lu, X. Cheng, J. Huang, and J. A. McCammon, *P. Natl. Acad. Sci. USA* **103**, 19314 (2006).
12. C. Bajaj, S.-C. Chen, and A. Rand, *SIAM J. Sci. Comput.* **33**, 826 (2011).
13. W. H. Geng and R. Krasny, *J. Comput. Phys.* **247**, 62 (2013).
14. C. D. Cooper, J. P. Bardhan, and L. A. Barba, *Comput. Phys. Commun.* **185**, 720 (2014), preprint on arXiv:/1309.4018.
15. P. B. Shaw, *Phys. Rev. A* **32**, 2476 (1985).
16. B. J. Yoon and A. M. Lenhoff, *J. Comput. Chem.* **11**, 1080 (1990).
17. A. H. Juffer, E. F. F. Botta, B. A. M. van Keulen, A. van der Ploeg, and H. J. C. Berendsen, *J. Comput. Phys.* **97**, 144 (1991).
18. L. Greengard and V. Rokhlin, *J. Comput. Phys.* **73**, 325 (1987).
19. L. F. Greengard and J. Huang, *J. Comp. Phys.* **180**, 642 (2002), ISSN 0021-9991, URL <http://www.sciencedirect.com/science/article/B6WHY-46G47HY-C/2/e30e42b51d48870e38c09e0713c52703>.
20. Z.-H. Duan and R. Krasny, *J. Comp. Chem.* **22**, 184 (2001).
21. P. Li, H. Johnston, and R. Krasny, *J. Comput. Phys.* **228**, 3858 (2009).
22. M. Bebendorf, *Numer. Math.* **86**, 565 (2000).
23. K. L. Ho and L. Greengard, *SIAM J. Sci. Comput.* **34**, A2507 (2012).
24. M. B. Giles and E. Sli, *Acta Numerica* 2002 p. 145236 (2002).

25. R. Becker and R. Rannacher, *An optimal control approach to a posteriori error estimation in finite element methods: Acta numerica* (2003).
26. D. Estep, SIAM Journal on Numerical Analysis **32**, 1 (1995).
27. K. Eriksson, D. Estep, P. Hansbo, and C. Johnson, *Computational Differential Equations* (Cambridge University Press, Cambridge, 1996), ISBN 0-521-56312-7; 0-521-56738-6.
28. D. J. Estep, M. G. Larson, R. D. Williams, and A. M. Society, *Estimating the error of numerical solutions of systems of reaction-diffusion equations* (American Mathematical Society, 2000).
29. J. H. Chaudhry, J. N. Shadid, and T. Wildey, Applied Numerical Mathematics **135**, 129 (2019).
30. W. Bangerth and R. Rannacher, *Adaptive Finite Element Methods for Differential Equations* (Birkhauser Verlag, 2003).
31. M. Ainsworth and T. Oden, *A posteriori error estimation in finite element analysis* (John Wiley-Teubner, 2000).
32. T. J. Barth, *A posteriori Error Estimation and Mesh Adaptivity for Finite Volume and Finite Element Methods*, vol. 41 of *Lecture Notes in Computational Science and Engineering* (Springer, New York, 2004).
33. J. Chaudhry, D. Estep, V. Ginting, J. Shadid, and S. Tavener, Computer Methods in Applied Mechanics and Engineering **285**, 730 (2015).
34. J. Collins, D. Estep, and S. Tavener, BIT Numerical Mathematics **55**, 1017 (2015).
35. A. Logg, Appl. Numer. Math. **48**, 339 (2004).
36. K. Eriksson, C. Johnson, and A. Logg, SIAM Journal on Scientific Computing **25**, 1142 (2004).
37. J. H. Chaudhry, J. Collins, and J. N. Shadid, Applied Numerical Mathematics **117**, 36 (2017).

38. J. Chaudhry, D. Estep, S. Tavener, V. Carey, and J. Sandelin, SIAM Journal on Numerical Analysis (2016).
39. J. Chaudhry, D. Estep, and S. Tavener, arXiv e-prints arXiv:1907.01139 (2019), 1907.01139.
40. B. Aksoylu, S. D. Bond, E. C. Cyr, and M. Holst, Journal of Scientific Computing **52**, 202 (2011), ISSN 1573-7691.
41. J. H. Chaudhry, SIAM Journal on Scientific Computing **40**, A2519 (2018).
42. C. Domnguez and N. Heuer, Numerical Methods for Partial Differential Equations **30**, 947 (2014).
43. N. Heuer and M. Karkulik, ESAIM: Mathematical Modelling and Numerical Analysis pp. 1193–1217 (2015).
44. S. Decherchi, M. Masetti, I. Vyalov, and W. Rocchia, European journal of medicinal chemistry **91**, 27 (2015).
45. W. Śmigaj, T. Betcke, S. Arridge, J. Phillips, and M. Schweiger, ACM Transactions on Mathematical Software (TOMS) **41**, 6 (2015).
46. M. F. Sanner, A. J. Olson, and J.-C. Spehner, in *Proceedings of the eleventh annual symposium on Computational geometry* (ACM, 1995), pp. 406–407.
47. S. Decherchi and W. Rocchia, PloS one **8**, e59744 (2013).
48. P. J. Roache, *Verification and validation in computational science and engineering* (Hermosa Albuquerque, 1998).
49. Z. Yu, M. J. Holst, Y. Cheng, and J. A. McCammon, Journal of Molecular Graphics and Modelling **26**, 1370 (2008).
50. J. G. Kirkwood, J. Chem. Phys. **2**, 351 (1934).
51. M. D. Altman, J. P. Bardhan, J. K. White, and B. Tidor, J. Comput. Chem. **30**, 132 (2009).

52. M. Martínez, C. D. Cooper, A. B. Poma, and H. V. Guzman, *Journal of Chemical Information and Modeling* **60**, 974 (2019).